The Astrophysical Journal Letters, 927:L22 (6pp), 2022 March 10 https://doi.org/10.3847/2041-8213/ac574e

Dust Resurgence in Protoplanetary Disks Due to Planetesimal–Planet Interactions

Lia Marta Bernabò[1,2], Diego Turrini[3], Leonardo Testi[4,5], Francesco Marzari[1], and Danai Polychroni[6]
[1] Department of Physics and Astronomy, University of Padova, Via Marzolo 8, I-35131 Padova, Italy; lia.bernabo@dlr.de
[2] Deutsches Zentrum für Luft- und Raumfahrt, Rutherfordstrasse 2, D-12489 Berlin, Germany
[3] INAF, Osservatorio Astrofisico di Torino, Via Osservatorio 20, I-10025, Pino Torinese, Italy
[4] European Southern Observatory, Karl-Schwarzschild-Str. 2, D-85748 Garching bei München, Germany
[5] INAF-Osservatorio Astrofisico di Arcetri, Largo E. Fermi 5, I-50125 Firenze, Italy
[6] Independent Researcher
Received 2021 December 2; revised 2022 February 17; accepted 2022 February 17; published 2022 March 10

Abstract

Observational data on the dust content of circumstellar disks show that the median dust content in disks around pre-main-sequence stars in nearby star-forming regions seems to increase from ∼1 to ∼2 Myr and then decline with time. This behavior challenges the models where the small dust grains steadily decline by accumulating into larger bodies and drifting inwards on a short timescale (⩽1 Myr). In this Letter we explore the possibility to reconcile this discrepancy in the framework of a model where the early formation of planets dynamically stirs the nearby planetesimals and causes high-energy impacts between them, resulting in the production of second-generation dust. We show that the observed dust evolution can be naturally explained by this process within a suite of representative disk-planet architectures.

Unified Astronomy Thesaurus concepts: Protoplanetary disks (1300); Planetary-disk interactions (2204); Planetary migration (2206); Collision processes (2065); Planetary system formation (1257); Planetesimals (1259); Circumstellar disks (235)

1. Introduction

Dust in protoplanetary disks is expected to rapidly settle on the midplane and grow to pebble sizes (e.g., Natta et al. 2007; Testi et al. 2014; Birnstiel et al. 2016), with subsequent growth to planetesimals and planetary cores then occurring through rapid accretion and instabilities (e.g., Johansen et al. 2014; Johansen & Lambrechts 2017; Johansen et al. 2019). In addition to the planet-formation route, dust can also progressively be removed from the outer regions of disks via gas-induced radial drift (e.g., Weidenschilling 1977; Birnstiel et al. 2016; Toci et al. 2021). ALMA surveys provide growing evidence for the rapid depletion of dust and early formation of planetary bodies in disk populations (e.g., Testi et al. 2016; Manara et al. 2018; Williams et al. 2019). However, one surprising result of the analysis of the ALMA disks survey data is the apparent lack of decay, and even increase, of the dust content in the first 1–3 Myr of disk evolution (e.g., Williams et al. 2019; Cazzoletti et al. 2019b; Testi et al. 2022). While planet-formation-induced substructures in the disk gas distribution may effectively create dust traps and slow down the dust drift, the concentration of dust in traps is expected to promote planetesimal growth and planet formation (e.g., Carrera et al. 2021; Eriksson et al. 2021). As a result, even in dust traps, the amount of dust in disks should steadily decrease over time.

The meteoritic constraints from the solar system also confirm that dust coagulation and the assembly of planetesimals has to occur on fast timescales of the order of 1 Myr or shorter (e.g., Scott 2007; Nittler & Ciesla 2016; Wadhwa et al. 2020). The dust content of the disk populations in star-forming regions with different ages should therefore show a rapid and monotonic decline of the dust content from ages ⩽1 Myr. However, the homogeneous analysis of ALMA data performed by Testi et al. (2022) appears to suggest that disks in star-forming regions with average stellar ages of 1 Myr or less possess a similar or lower median dust content compared to older 2–3 Myr disks (see also the discussion in Williams et al. 2019; Cazzoletti et al. 2019b). While these results are still uncertain and rely on the assumptions that the dust properties and conversion factors from observed millimeter flux, as well as the dust mass, remain constant across disk evolution around pre-main-sequence stars (see discussion in Testi et al. 2022), the expected significant monotonic decrease in median dust mass seems to begin only after 2–3 Myr.

In this work, we explore a possible explanation for this apparently contradictory observational result and show that the observations are indeed consistent with the expectations from planet formation. Specifically, as discussed in Turrini et al. (2012, 2019) and Gerbig et al. (2019) the classical view of dust evolution in disks ignores the dynamical and collisional effects of planetesimal–planet interactions. Turrini et al. (2019) showed in the case of the disk around HD 163296 that the formation of massive planets triggers a phase of strong dynamical excitation of the planetesimal population embedded in the disk, leading to eccentric orbits, high collisional probabilities, and dust production. The apparent rise of the dust median values at around ∼2 Myr and the following decrease may thus be a consequence of the planet-formation process and its dynamical effects on the disk.

In this Letter, we compare the median dust-mass estimates from millimeter observations of disks in different star-forming regions characterized by various ages with the predicted dust content evolution in disks based on theoretical models that include the formation of second-generation dust produced by planetesimal collisions. In particular, we focus on planets massive enough to dynamically stir the planetesimal disk: this

definition roughly encompasses all planets more massive than a few Earth masses independently of the specific type of planet. Our results illustrate that the observed median dust evolution is well reproduced by models that consider the collisional evolution of planetesimals in systems characterized by a representative set of common planetary architectures.

2. Observational Data: Dust Mass versus Age

The dust-mass content in large samples of protoplanetary disks is now available thanks to the observations by the Atacama Large Millimeter/submillimeter Array (ALMA). In this work, we focus on the dust-mass estimates in disks populating the following star-forming regions, ordered by age: Corona Australis region (Cazzoletti et al. 2019a) aged 0.6 Myr, Taurus region (Akeson et al. 2019) aged 0.9 Myr, L1688 region (Testi et al. 2016, 2022; Williams et al. 2019) aged 1.0 Myr, Lupus region (Ansdell et al. 2018) aged 2.0 Myr, Chamaeleon region (Pascucci et al. 2016) aged 2.8 Myr, and Upper Scorpius region (Barenfeld et al. 2016) aged 4.3 Myr. For all these regions we use the compilations of Testi et al. (2022), which include a homogeneous recalculation of the disk mass and the adoption of GAIA distances and membership analyses. The median ages we use for each of the stellar populations are also computed in Testi et al. (2022). Due to the possible dependence of the disk evolution on the initial disk mass and, therefore, on the stellar mass, we focus our analysis on two specific mass groups. The first group contains disks around solar-type stars with masses in the range $0.5M_{\oplus} \leqslant M_{*} \leqslant 1.6M_{\oplus}$, while the second group contains disks around red dwarf stars with masses in the range $0.2M_{\oplus} \leqslant M_{*} \leqslant 0.4M_{\oplus}$.

Figure 2 shows the estimated dust masses plotted versus the median age of the star-forming region in the two stellar-mass groups. The data in this figure clearly show that the dust content in disks increases between ∼0.5–1 Myr and ∼2Myr, then declines monotonically only after about 2–3 Myr, instead of the expected fast decay due to the combined effects of grain growth, radial drift, and accretion.

3. Numerical Model of Dust Rejuvenation

The *n*-body simulations are performed with the code MERCURY-ARχES (Turrini et al. 2019, 2021a), which allows us to model the effects of the mass growth and orbital migration of forming middle-mass and massive planets on the dynamical evolution of planetesimals alongside those of gas drag and disk self-gravity. The setup of the *n*-body simulations follows those adopted in Turrini et al. (2019, 2021a), with the planetesimal disk extending up to the characteristic radius of the host protoplanetary disk. We adopt characteristic radii r_c of 30 au for the disks around red dwarf stars and 50 au for those around solar-type stars and describe the gas surface density with the exponentially tapered power law $\Sigma(r) = \Sigma_0\ (r/r_c)^{-\gamma} \exp\left[-(r/r_c)^{(2-\gamma)}\right]$. We adopt an exponent $\gamma = 0.8$ (Isella et al. 2016), with the gas surface density at the characteristic radius set at 5.9 and 22.7 g cm^{-2} respectively. This choice results in disks of 0.003 and 0.03 $M_{\odot}$ around red dwarf and solar-type stars, respectively. The masses of the central stars were set to 0.3 $M_{\odot}$ for red dwarf stars and 1 $M_{\odot}$ for solar-type stars. We set the spatial density of massless particles in the *n*-body simulations to 1000 particles au^{-1}, with the inner edge of the planetesimal disk at 1 au and the outer edge at r_c.

The damping effects of gas drag on massless particles are simulated following the treatment from Brasser et al. (2007) with updated drag coefficients from Nagasawa et al. (2019). The exciting effects of disk self-gravity are simulated based on the analytical treatment of axisymmetric disks by Ward (1981) following Marzari (2018) and Nagasawa et al. (2019) (see Turrini et al. 2021a for further discussion). The *n*-body simulations account for the formation of gaps around gas-giant planets, as discussed below, but do not include the effects of nonaxisymmetric perturbations, like spiral arms. The disk gas mass does not decline over time and is constant across the *n*-body simulations except inside the gaps (see below). Because nonaxisymmetric perturbations would increase the planetesimal dynamical excitation by promoting higher eccentricity in their orbits (see, e.g., Marzari et al. 2013 for an illustrative discussion) and because the damping effects of gas drag dominate over the disk self-gravity (e.g., Nagasawa et al. 2019; Turrini et al. 2021a) and depend on the gas density, our simulations provide a conservative estimate of the dynamical excitation of the planetesimals. In computing the dynamical effects of the disk gas in the *n*-body simulations, all massless particles are characterized by a diameter of 100 km (see Klahr & Schreiber 2016; Johansen & Lambrechts 2017; Turrini et al. 2019) and a density of 1 g cm^{-3} (see Turrini et al. 2019, 2021a).

The formation of the planets is modeled over two growth phases (Lissauer et al. 2009; D'Angelo et al. 2010; Bitsch et al. 2015; Johansen & Lambrechts 2017; Johansen et al. 2019; D'Angelo et al. 2021) using the parametric approach from Turrini et al. (2011, 2019, 2021a). The first phase is common to all planets, from super-Earths to gas giants, and accounts for their growth by pebble and planetesimal accretion (Bitsch et al. 2015; Johansen & Lambrechts 2017; Johansen et al. 2019). The planetary mass evolves as $M_p(t) = M_0 + \left(\frac{e}{e-1}\right)(M_1 - M_0)(1 - e^{-t/\tau_p})$, where $M_0 = 0.01\ M_{\oplus}$ is the initial mass of the planetary seed (Johansen & Lambrechts 2017; Johansen et al. 2019), M_1 is the final mass at the end of the first growth phase, and e is the Euler number. M_1 is set to 30 $M_{\oplus}$ for gas giants (i.e., planets with final mass >30 $M_{\oplus}$) while it matches the final planetary mass in all other cases (i.e., planets with final masses ⩽30 $M_{\oplus}$; see Table 1 for the specific values). The constant τ_p is the duration of the first growth phase and is set to 1 Myr for all planets based on observational (Manara et al. 2018) and theoretical constraints on the characteristic timescale for pebble accretion (Johansen & Lambrechts 2017; Johansen et al. 2019).

Gas giants also undergo the second phase of mass growth, accounting for their runaway gas accretion, where their mass evolves as $M_p(t) = M_1 + (M_2 - M_1)(1 - e^{-(t-\tau_p)/\tau_g})$, where M_2 is the final mass of the gas-giant planet and τ_g is the e-folding time of the runaway gas accretion process. The value of τ_g is set to 0.1 Myr based on the results of hydrodynamic simulations (Lissauer et al. 2009; D'Angelo et al. 2010, 2021), meaning that the gas giants reach more than 99% of their final mass in about 0.5 Myr from the onset of the runaway gas accretion. During the runaway gas accretion process, giant planets form a gap in the disk gas whose width is modeled as $W_{\rm gap} = C \cdot R_H$ (Isella et al. 2016; Marzari 2018), where the numerical proportionality factor $C = 8$ is assumed following Isella et al. (2016). The gas density $\Sigma_{\rm gap}(r)$ inside the gap evolves over time with respect to the local unperturbed gas density $\Sigma(r)$ as $\Sigma_{gap}(r) = \Sigma(r) \cdot \exp\left[-(t - \tau_p)/\tau_g\right]$ (Turrini et al. 2021a).

The migration of growing planets is modeled over two migration phases based on the migration tracks from Mordasini et al. (2015)

Table 1
The Set of Representative Disk-planet Architectures Used in the Simulations of This Study

Scenario	Stellar Mass	Characteristic Radius R_c	Initial Mass of Dust	Planetary Mass	Semimajor Axis	
Run 1	1 $M_\odot$	50 au	100 $M_\oplus$	1 $M_{\rm Jup}$	5 au, 11 au	
Run 2	1 $M_\odot$	50 au	100 $M_\oplus$	1 $M_{\rm Jup}$	5 au, 11 au, 22 au	
Run 3	1 $M_\odot$	50 au	100 $M_\oplus$	150 $M_\oplus$	5 au, 11 au	
Run 4	1 $M_\odot$	50 au	100 $M_\oplus$	150 $M_\oplus$	5 au, 11 au, 22 au	
Run 5	0.3 $M_\odot$	30 au	10 $M_\oplus$	30 $M_\oplus$	5 au 8 au	
Run 6	0.3 $M_\odot$	30 au	10 $M_\oplus$	10 $M_\oplus$	5 au, 8 au, 11 au	
					Initial semimajor axis	Final semimajor axis
Run 7	1 $M_\odot$	50 au	100 $M_\oplus$	1 $M_{\rm Jup}$	5 au	0.5 au
Run 8	1 $M_\odot$	50 au	100 $M_\oplus$	1 $M_{\rm Jup}$	11 au	0.5 au
Run 9	1 $M_\odot$	50 au	100 $M_\oplus$	1 $M_{\rm Jup}$	22 au	0.5 au
Run 10	0.3 $M_\odot$	30 au	10 $M_\oplus$	30 $M_\oplus$	11 au	0.5 au
Run 11	0.3 $M_\odot$	30 au	10 $M_\oplus$	30 $M_\oplus$	8 au, 11 au	0.5 au
Run 12	0.3 $M_\odot$	30 au	10 $M_\oplus$	30 $M_\oplus$	8 au	0.5 au
Run 13	0.3 $M_\odot$	30 au	10 $M_\oplus$	10 $M_\oplus$	11 au	0.5 au
Run 14	0.3 $M_\odot$	30 au	10 $M_\oplus$	10 $M_\oplus$	8 au, 11 au	0.5 au

Note. The values reported are those at the beginning of the simulations, which correspond to 0.2 Myr old disks. When multiple initial semimajor axes are reported, their number matches the number of massive planets considered in that specific scenario. When a final semimajor axis is specified (runs 7–14), the simulation includes orbital migration otherwise the planets are assumed to form in situ (runs 1–6).

following the parametric approach from Turrini et al. (2021a). During the first growth phase, all planets undergo a linear migration regime with drift rate (Hahn & Malhotra 2005; Turrini et al. 2021a) $\Delta v_1 = \frac{1}{2}\frac{\Delta a_1}{a_p}\frac{\Delta t}{\tau_p} v_p$, where Δt is the time step of the n-body simulation, Δa_1 is the radial displacement during the first growth phase, and v_p and a_p are the instantaneous planetary orbital velocity and semimajor axis, respectively. During the second growth phase, gas giants undergo a power-law migration regime with drift rate (Hahn & Malhotra 2005; Turrini et al. 2021a) $\Delta v_2 = \frac{1}{2}\frac{\Delta a_2}{a_p}\frac{\Delta t}{\tau_g}\exp^{-(t-\tau_c)/\tau_g} v_p$, where Δa_2 is the radial displacement during the second growth phase. In the simulations involving migrating planets (runs 7–14; see Table 1) the final semimajor axis of the innermost planet is always set to 0.5 au. In the case of gas giants, 40% of the radial displacement occurs during the first growth phase and 60% during the second growth phase (Turrini et al. 2021a). In all other cases, the whole radial displacement occurs during the first growth phase.

The orbital elements of massless particles are recorded every 0.1 Myr and the impact probabilities among them are computed by means of the statistical model by Wetherill (1967), Greenberg et al. (1988), and Farinella & Davis (1992), widely used in collisional studies of the asteroid belt (O'Brien & Sykes 2011). The collisional frequencies and the dust production rates over each 0.1 Myr long time interval are estimated following the approach by Turrini et al. (2019) based on the scaling law for the collisional mass erosion by Genda et al. (2017). We assume that 20% of the eroded mass is eventually converted into dust by the collisional cascade due to the increased dust production efficiency of smaller impactors (O'Keefe & Ahrens 1985; Koschny & Grün 2001; see Turrini et al. 2019 for discussion). The dust production is computed with the parallel code DEBRIS using a particle-based approach instead of the original grid-based approach by Turrini et al. (2019), as the latter is not accurate in the presence of migrating planets. In computing the dust production, each massless particle in the n-body simulations is treated as a swarm of planetesimals.

The initial mass of each swarm is computed by integrating the disk gas density profile over a ring 0.1 au wide centered on the initial orbit of the massless particle and assuming a dust-to-gas ratio of 0.01 (e.g., Bohlin et al. 1978; Natta et al. 2007; Ercolano & Pascucci 2017). This results in disks initially containing 110 and 10 $M_\oplus$ of dust around solar-type and red dwarf stars, respectively. The bulk of the initial dust population is assumed to be converted into planetesimals by the time the disks become dynamically excited, as discussed below. The size-frequency distribution of the planetesimals in each swarm is that characteristic of a population in a collisional steady-state (Weidenschilling 2008, 2011 see Turrini et al. 2019, for a discussion), with diameters spanning between 1 m and 400 km (Krivov et al. 2018; Turrini et al. 2019). The total mass of each swam decreases over time from its initial value due to the mass loss associated with the collisional dust production. This approach allows the self-regulating nature of the collisional process under study to be captured without having to fully resolve the collisional cascade (Turrini et al. 2019): as a result, the more intense the dust production, the faster the depletion of the population of excited planetesimals, which in turn implies a shorter duration of the collisional dust production phase.

The n-body simulations start from the time the 0.01 $M_\oplus$ seeds appear in the disks. To compare the simulated systems with the observed data, we assume that such planetary seeds form in $t_0 = 0.5$ Myr. By 1 Myr in the timescale of the observed systems (hence, 0.5 Myr in the timescale of the simulations), the simulated disks will contain planets at least a few $M_\oplus$ in mass, more than 90% of the initial dust population will be incorporated into planetesimals (see the curves labeled "planetesimal formation" in Figure 2 and Section 4 for further discussion), and the planetesimals will start being dynamically excited by the planets (see Figure 1). The dust produced over each 0.1 Myr long interval is added to the existing dust population, and the resulting total dust declines with time following a power law with a characteristic timescale of $\simeq$1.5 Myr to account for the continuing dust evolution and the decreasing efficiency of planetesimal formation over time (see

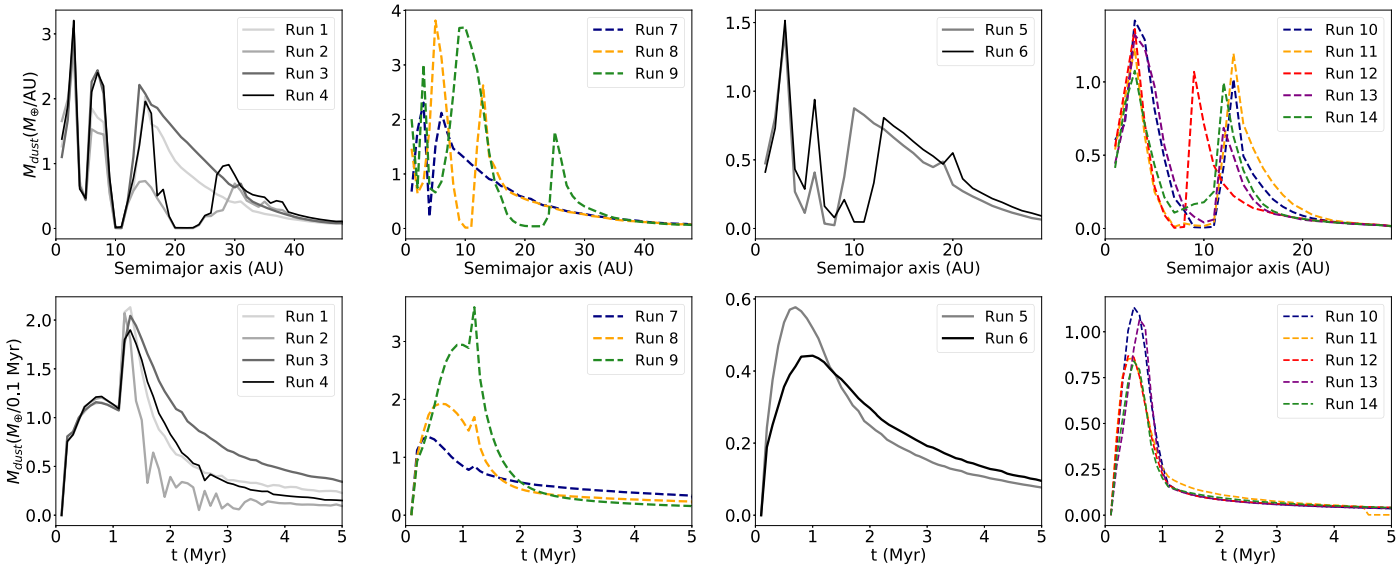

Figure 1. The plots show the dust production across the radial extension of the disk (in $M_\oplus$ per 1 au wide ring integrated over time, top row) and across time (in $M_\oplus$ produced every 0.1 Myr spatially integrated over the whole disk, bottom row) for all runs. In both rows, the plots show the dust production for planets forming in situ (first and third panels) and for migrating planets (second and fourth panels). The first two panels in each row refer to solar-type stars, the last two to red dwarf stars.

Johansen et al. 2019 for a discussion). The total dust-mass evolution with time can then be compared with the observed data.

The set of scenarios considered for both solar-type and red dwarf stars, summarized in Table 1, encompasses architectures with two or three "cold" planets forming in situ as well as with one or two planets migrating across the disk from different starting positions to become "hot" planets. This choice is motivated by the goal of comparing the median dust evolution of the observed disk populations with a set of planet-forming scenarios that are representative, within the limits of our current observational capabilities, of common planetary architectures among exoplanets. As a result, we focused our exploration on planetary systems hosting one to three planets: although this may be an observational bias, single-planet systems currently account for the majority of known exoplanetary systems (source: The Extrasolar Planets Encyclopaedia[7]), while planetary systems hosting two to three planets dominate the known population of multiplanet systems (Zinzi & Turrini 2017; Turrini et al. 2020). Furthermore, the semimajor axes of the migrating and nonmigrating planets we considered span the orbital range (∼0.1–20 au), where the vast majority of the currently confirmed exoplanets reside (source: NASA Exoplanet Archive[8]).

4. Comparison between Model Results and Observations

Figure 1 illustrates the collisional dust production in the simulated planet-forming scenarios reported in Table 1 plotted as a function of the radial distance (top panels) and time (bottom panels). In Figure 2 we compare the dust observed in the considered disk population with the predictions of our simulations of dust rejuvenation. The simulated dust production scenarios are capable of successfully reproducing the regrowth and slower decline of the dust content revealed by observational data. The initial rapid decline of dust content before 1 Myr, due to the dust growth into planetesimals, is followed by a rise in dust production linked to the appearance of the planets and the high-velocity collisions among planetesimals they create. The secular evolution of the dust, combined with the decline of the population of excited planetesimals due to collisional erosion and gas drag, naturally explains the secular, slow decay of the dust-mass content with time observed in the considered disk populations.

As illustrated in the top panels of Figure 1 the dust rejuvenation process can affect a significant fraction of the radial extension of circumstellar disks. In the simulated scenarios and for the assumed dust production efficiency, planetesimal impacts can convert between 25% and 50% of the mass of the planetesimal disk back into dust. As dust production linearly depends on the dust production efficiency and the mass of the planetesimal disk, our results can be readily scaled to different values of the latter quantities. As discussed in Section 3, our scenarios assume an efficient conversion of the initial dust budget into planetesimals to fit the observational data. Lower planetesimal formation efficiencies would proportionally reduce the collisional production of dust and the overall dust population at later ages and would result in disks containing varying mixtures of primordial and second-generation dust (Turrini et al. 2019). Disks characterized by very low planetesimal formation efficiency (e.g., ∼10%) would result in limited collisional dust production. However, such a scenario would be at odds with the observed dust masses of disks between 1 and 2 Myr (Testi et al. 2022), as well as with the masses of known exoplanetary systems (Testi et al. 2016; Manara et al. 2018; Mulders et al. 2021) and the metallicities of known giant planets (Thorngren et al. 2016; Shibata et al. 2020; Turrini et al. 2021a, 2021b). The duration of the dust rejuvenation process in our simulations ranges between 1 and 2 Myr, depending on the formation history of the system (see Figure 1, bottom panels). This duration matches well with the age interval of observed disks with a rising dust population (see Figure 2). As illustrated by the presence of two peaks in dust production over time due to forming gas giants (see in particular the bottom-left panel of Figure 1), the dust rejuvenation process is triggered already when planets of a few

[7] http://exoplanet.eu
[8] https://exoplanetarchive.ipac.caltech.edu

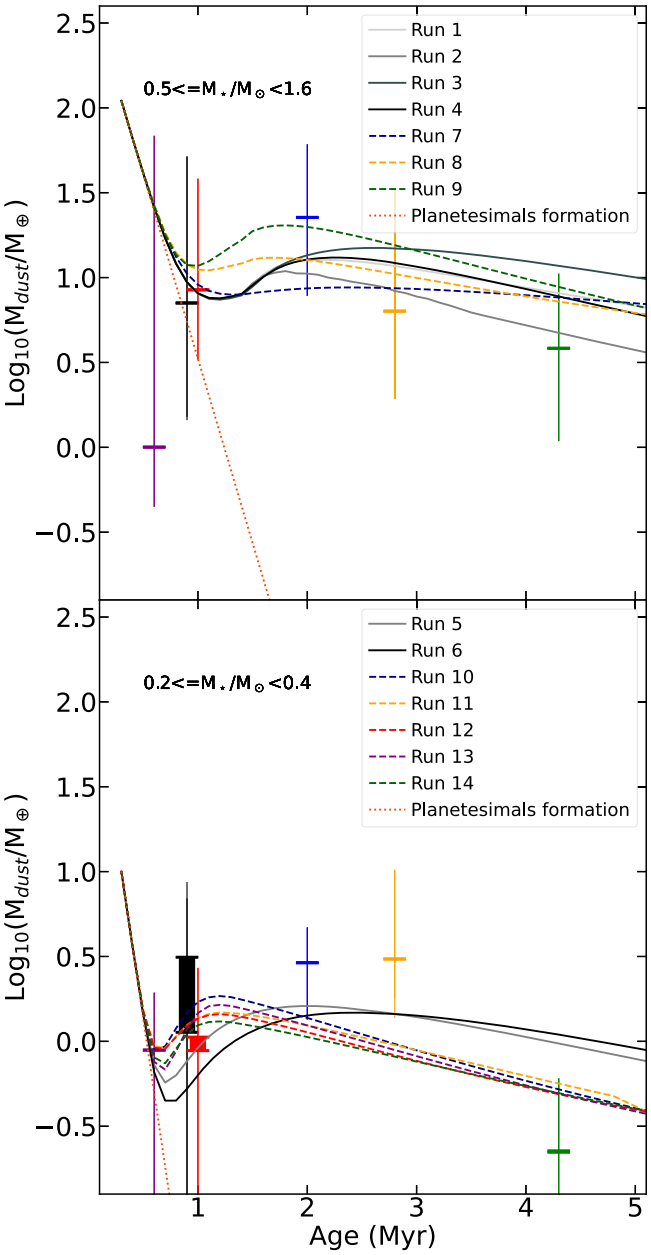

Figure 2. Dust mass vs. age of the star-forming region for disks around solar-type stars (top panel) and red dwarf stars (bottom panel). For each star-forming region, the thin vertical lines highlight the 25th and 75th percentiles, while the horizontal line marks the median value. The thick vertical bars, where present, show the possible range of median values (see Testi et al. 2022 for a detailed explanation of how the range is computed). The red dotted line shows the expected dust decrease due to the formation of planetesimals when no dust rejuvenation is included.

$M_\oplus$ in mass are present within circumstellar disks, although the dust production is less intense than when giant planets appear.

As shown in Figures 1 and 2, the spatial distribution and temporal evolution of the dust rejuvenation process strongly depend on the architecture and formation history of the simulated systems. Circumstellar disks hosting significantly less massive planets than those here considered may be affected by limited dust rejuvenation, making their dust population indistinguishable from that of disks that host no planet. Alternatively, their dust rejuvenation could be characterized by a short peak duration followed by a rapid decline, resulting in curves crossing the low-end tails of the dust distributions observed in Chamaeleon and Upper Scorpius (see Figure 2). Conversely, systems characterized by more extreme migration histories of gas giants (as recently suggested for the solar system by Öberg & Wordsworth 2019; Pirani et al. 2019, and V1298 Tau by Suárez Mascareño et al. 2021) or higher multiplicities of migrating planets (e.g., Trappist-1 in the case of red dwarf stars, Tamayo et al. 2017; Papaloizou et al. 2018; and the solar system, Pirani et al. 2019) could be characterized by stronger dust rejuvenation processes and produce dust populations consistent with the high-end values observed in Lupus and Chamaeleon (see Figure 2).

5. Conclusions

The fast decay of dust mass in circumstellar disks expected on the basis of grain growth and radial drift is not observed in the surveys of circumstellar disks of different ages by ALMA. A possible explanation for the delayed disappearance of the dust is the formation of second-generation dust by planetesimal collisions excited by the formation of planets more massive than a few $M_\oplus$, the specific mass values depending on the architecture of individual systems. The models we presented for the rejuvenation of the dust content in disks closely match the observations and provide strong support to the scenario where the formation of planets can lead to a resurgence of the dust mass. This process increases the lifetime of the dust component of circumstellar disks, delaying the final disappearance of the dust to after the formation of the planets. Within this scenario, the observational data on the dust abundances of disks in star-forming regions of different ages indicate that the timescale for the complete formation of planets can be directly constrained by the peaks in the dust abundances to $\leqslant$1–2 Myr. Finally, the phase of intense planetesimal collisions linked to the formation of planets and the associated collisional erosion of the larger planetesimals can provide a natural mechanism to produce the large population of small planetesimals invoked by Krivov & Wyatt (2021) to explain the estimated dust masses in the population of debris disks.

This work was partly supported by the Italian Ministero dell'Istruzione, Università e Ricerca through the grant Progetti Premiali 2012-iALMA (CUP C52I13000140001), by the Deutsche Forschungsgemeinschaft (DFG, German Research Foundation) - Ref no. 325594231 FOR 2634/1 TE 1024/1-1, by the DFG Cluster of Excellence Origins (www.origins-cluster.de) and by the Italian National Institute of Astrophysics (INAF) through the projects PRIN-INAF 2016 "The Cradle of Life - GENESIS-SKA (General Conditions in Early Planetary Systems for the rise of life with SKA)," PRIN-INAF 2019 "Planetary systems at young ages (PLATEA)," and the INAF Main Stream projects "Ariel and the astrochemical link between circumstellar discs and planets" (CUP: C54I19000700005) and "Non-spherical dust dynamics in proto-planetary disks: how dust particle realistic shapes change the dust evolution timescales" (CUP: C54I19000460005). This project has received funding from the European Union's Horizon 2020 research and innovation program under the Marie Sklodowska-Curie grant agreement No 823823 (DUSTBUSTERS) and from the European Research Council (ERC) via the ERC Synergy Grant ECOGAL (grant 855130). The computational resources for this work were supplied by the Genesis cluster at INAF-IAPS and the authors wish to thank Romolo Politi, Scige John Liu, Sergio Fonte, and Francesco Reale for their assistance with the computational

resources. This research has made use of the NASA Astrophysics Data System Bibliographic Services.

ORCID iDs

Lia Marta Bernabò https://orcid.org/0000-0002-8035-1032
Diego Turrini https://orcid.org/0000-0002-1923-7740
Leonardo Testi https://orcid.org/0000-0003-1859-3070
Francesco Marzari https://orcid.org/0000-0003-0724-9987
Danai Polychroni https://orcid.org/0000-0002-7657-7418

References

Akeson, R. L., Jensen, E. L. N., Carpenter, J., et al. 2019, ApJ, 872, 158
Ansdell, M., Williams, J. P., Trapman, L., et al. 2018, ApJL, 859, 21
Barenfeld, S. A., Carpenter, J. M., Ricci, L., & Isella, A. 2016, ApJL, 827, 142
Birnstiel, T., Fang, M., & Johansen, A. 2016, SSRv, 205, 41
Bitsch, B., Lambrechts, M., & Johansen, A. 2015, A&A, 582, A112
Bohlin, R. C., Savage, B. D., & Drake, J. F. 1978, ApJ, 224, 132
Brasser, R., Duncan, M. J., & Levison, H. F. 2007, Icar, 191, 413
Carrera, D., Simon, J. B., Li, R., Kretke, K. A., & Klahr, H. 2021, AJ, 161, 96
Cazzoletti, P., Manara, C. F., Baobab Liu, H., et al. 2019a, A&A, 626, A11
Cazzoletti, P., Manara, C. F., Liu, H. B., et al. 2019b, A&A, 626, A11
D'Angelo, G., Durisen, R. H., & Lissauer, J. J. 2010, in Exoplanets, ed. S. Seager (Tucson, AZ: Univ. of Arizona Press), 319
D'Angelo, G., Weidenschilling, S. J., Lissauer, J. J., & Bodenheimer, P. 2021, Icar, 355, 114087
Ercolano, B., & Pascucci, I. 2017, RSOS, 4, 170114
Eriksson, L. E. J., Ronnet, T., & Johansen, A. 2021, A&A, 648, A112
Farinella, P., & Davis, D. R. 1992, Icar, 97, 111
Genda, H., Fujita, T., Kobayashi, H., et al. 2017, Icar, 294, 234
Gerbig, K., Lenz, C. T., & Klahr, H. 2019, A&A, 629, A116
Greenberg, R., Carusi, A., & Valsecchi, G. B. 1988, Icar, 75, 1
Hahn, J. M., & Malhotra, R. 2005, AJ, 130, 2392
Isella, A., Guidi, G., Testi, L., et al. 2016, PhRvL, 117, 251101
Johansen, A., Blum, J., Tanaka, H., et al. 2014, in Protostars and Planets VI, ed. H. Beuther et al. (Tucson, AZ: Univ. of Arizona Press), 547
Johansen, A., Ida, S., & Brasser, R. 2019, A&A, 622, A202
Johansen, A., & Lambrechts, M. 2017, AREPS, 45, 359
Klahr, H., & Schreiber, A. 2016, in Proceedings of the International Astronomical Union, IAU Symposium, 318, Asteroids: New Observations, ed. S. R. Chesley et al. (Cambridge: Cambridge Univ. Press), 1
Koschny, D., & Grün, E. 2001, Icar, 154, 402
Krivov, A. V., Ide, A., Löhne, T., Johansen, A., & Blum, J. 2018, MNRAS, 474, 2564
Krivov, A. V., & Wyatt, M. C. 2021, MNRAS, 500, 718
Lissauer, J. J., Hubickyj, O., D'Angelo, G., & Bodenheimer, P. 2009, Icar, 199, 338
Manara, C. F., Morbidelli, A., & Guillot, T. 2018, A&A, 618, L3
Marzari, F. 2018, A&A, 611, A37
Marzari, F., Thebault, P., Scholl, H., Picogna, G., & Baruteau, C. 2013, A&A, 553, A71
Mordasini, C., Mollière, P., Dittkrist, K. M., Jin, S., & Alibert, Y. 2015, IJAsB, 14, 201
Mulders, G. D., Pascucci, I., Ciesla, F. J., & Fernandes, R. B. 2021, ApJ, 920, 66
Nagasawa, M., Tanaka, K. K., Tanaka, H., et al. 2019, ApJ, 871, 110
Natta, A., Testi, L., Calvet, N., et al. 2007, in Protostars and Planets V, ed. B. Reipurth, D. Jewitt, & K. Keil (Tucson, AZ: Univ. of Arizona Press), 767
Nittler, L. R., & Ciesla, F. 2016, ARA&A, 54, 53
Öberg, K. I., & Wordsworth, R. 2019, AJ, 158, 194
O'Brien, D. P., & Sykes, M. V. 2011, SSRv, 163, 41
O'Keefe, J. D., & Ahrens, T. J. 1985, Icar, 62, 328
Papaloizou, J. C. B., Szuszkiewicz, E., & Terquem, C. 2018, MNRAS, 476, 5032
Pascucci, I., Testi, L., Herczeg, G. J., et al. 2016, ApJL, 831, 125
Pirani, S., Johansen, A., Bitsch, B., Mustill, A. J., & Turrini, D. 2019, A&A, 623, A169
Scott, E. R. D. 2007, AREPS, 35, 577
Shibata, S., Helled, R., & Ikoma, M. 2020, A&A, 633, A33
Suárez Mascareño, A., Damasso, M., Lodieu, N., et al. 2021, NatAs, 6, 232
Tamayo, D., Rein, H., Petrovich, C., & Murray, N. 2017, ApJL, 840, L19
Testi, L., Birnstiel, T., Ricci, L., et al. 2014, in Protostars and Planets VI, ed. H. Beuther et al. (Tucson, AZ: Univ. Arizona Press), 339
Testi, L., Natta, A., Manara, C. F., et al. 2022, arXiv:2201.04079
Testi, L., Natta, A., Scholz, A., et al. 2016, A&A, 593, A111
Thorngren, D. P., Fortney, J. J., Murray-Clay, R. A., & Lopez, E. D. 2016, ApJ, 831, 64
Toci, C., Rosotti, G., Lodato, G., Testi, L., & Trapman, L. 2021, MNRAS, 507, 818
Turrini, D., Codella, C., Danielski, C., et al. 2021b, ExA
Turrini, D., Coradini, A., & Magni, G. 2012, ApJ, 750, 8
Turrini, D., Magni, G., & Coradini, A. 2011, MNRAS, 413, 2439
Turrini, D., Marzari, F., Polychroni, D., & Testi, L. 2019, ApJ, 877, 50
Turrini, D., Schisano, E., Fonte, S., et al. 2021a, ApJ, 909, 40
Turrini, D., Zinzi, A., & Belinchon, J. A. 2020, A&A, 636, A53
Wadhwa, M., McCoy, T. J., & Schrader, D. L. 2020, AREPS, 48, 233
Ward, W. R. 1981, Icar, 47, 234
Weidenschilling, S. J. 1977, MNRAS, 180, 57
Weidenschilling, S. J. 2008, PhyS, 130, 014021
Weidenschilling, S. J. 2011, Icar, 214, 671
Wetherill, G. W. 1967, JGR, 72, 2429
Williams, J. P., Cieza, L., Hales, A., et al. 2019, ApJL, 875, L9
Zinzi, A., & Turrini, D. 2017, A&A, 605, L4